

A Census of the Low Accretors. II: Accretion Properties

THANAWUTH THANATHIBODEE ^{1,2} BRANDON MOLINA ^{3,4} JAVIER SERNA ⁵ NURIA CALVET ¹ JESÚS HERNÁNDEZ ⁵,
JAMES MUZEROLLE ⁶ AND RAMIRO FRANCO-HERNÁNDEZ ⁷

¹*Department of Astronomy, University of Michigan, 1085 South University Ave., Ann Arbor, MI 48109, USA*

²*Institute for Astrophysical Research, Department of Astronomy, Boston University, 725 Commonwealth Ave., Boston, MA 02215, USA*

³*Department of Climate and Space Sciences and Engineering, University of Michigan, 2455 Hayward St., Ann Arbor, MI 48109, USA*

⁴*Department of Atmospheric and Oceanic Sciences, University of Colorado, 311 UCB, Boulder, CO 80309, USA*

⁵*Instituto de Astronomía, Universidad Nacional Autónoma de México, Ensenada, México*

⁶*Space Telescope Science Institute, 3700 San Martin Dr., Baltimore, MD 21218, USA*

⁷*Instituto de Astronomía y Meteorología, Universidad de Guadalajara, Avenida Vallarta No. 2602, Col. Arcos Vallarta, CP 44130, Guadalajara, Jalisco, Mexico*

(Received May 14, 2022; Revised December 14, 2022; Accepted December 15, 2022)

Submitted to ApJ

ABSTRACT

Much is known about the processes driving accretion from protoplanetary disks onto low-mass pre-main-sequence stars (T Tauri stars). Nevertheless, it is unclear how accretion stops. To determine the accretion properties and their relation to stellar properties and gain insight into the last stages of accretion, we present a detailed analysis of 24 low and possible accretors, previously identified using the He I $\lambda 10830$ line. We model moderate-resolution H α profiles of these stars using magnetospheric accretion flow models that account for the chromospheric contribution at the line center. Based on parameters derived from the fits of 20 stars that can be reproduced with the models, we find a power-law relation between the disk truncation radius and the mass accretion rate consistent with predictions from theory and simulations. Comparing the corotation and truncation radii, we find that most of our targets are accreting in the unstable regime and rule out the propeller as the main process stopping accretion. For the truncation radius to be the same as the magnetic radius, the dipole magnetic field and/or the efficiency parameter ξ need to be smaller than previously determined, suggesting that higher-order fields dominate in low accretion rates. Lastly, we determine that the lowest accretion rates that can be detected by H α line modeling are $1 - 3 \times 10^{-11} M_{\odot} yr^{-1}$ for M3 stars and $3 - 5 \times 10^{-11} M_{\odot} yr^{-1}$ for K5 stars. These limits are lower than the observed accretion rates in our sample, suggesting that we have reached a physical lower limit. This limit, $\dot{M} \sim 10^{-10} M_{\odot} yr^{-1}$, is consistent with EUV-dominated photoevaporation.

Keywords: Accretion, H I line emission, Protoplanetary disks, T Tauri stars

1. INTRODUCTION

Detailed modeling of emission line profiles of accreting T Tauri stars (TTS) provides valuable information on accretion properties such as mass accretion rate and accretion geometry (e.g., Muzerolle et al. 2001; Lima et al. 2010; Kurosawa et al. 2011; Alencar et al. 2012; Thanathibodee et al. 2019, 2020). Comparing the stellar properties with the accretion properties of stars and

disks provides insight into the star and disk connection, as well as their evolution (e.g., Manara et al. 2016, 2017b; Alcalá et al. 2017).

In an effort to understand the last stages of the evolution of stellar accretion, we have conducted a survey to search for T Tauri stars near the end of their accretion phase – the low accretors. These stars still host primordial dust disks at different stages of evolution, but their signatures of mass accretion onto the stars are very weak, indicating that the mass accretion onto these stars has nearly stopped. Using a sensitive probe of accretion – the He I $\lambda 10830$ line – we identified 51 stars accreting at very low but unknown rates (Thanathibodee

et al. 2022; hereafter Paper I). We found correlations between accretion properties derived from the He I line and properties of the disks, and in particular, we found that accreting stars, albeit at very low rates, still have dust in the inner disk. We also found evidence that the processes stopping accretion may not be directly related to the stellar mass, suggesting that common processes ending accretion may occur in a wide range of masses.

Although qualitative comparisons between the He I $\lambda 10830$ accretion signature and properties of the disks and the stars have provided us with some insight into the last stages of accretion, a more quantitative analysis is needed to get the full picture. In particular, the He I line, although sensitive to accretion, does not provide the measurement of the mass accretion rates or the geometry of accretion. However, this information can be obtained by detailed modeling of emission lines formed in the accretion flows using the magnetospheric accretion model.

Here we report observations and magnetospheric accretion flows modeling of 22 newly identified low accretors and 2 possible accretors to search for correlations between accretion properties and properties of stars and the disks. By quantitatively analyzing the mass accretion rates and geometry, we aim to gain some insight into the last stages of stellar accretion.

This paper is organized as follows. In § 2 we describe the observations and data sources. In § 3 we derive stellar properties, apply magnetospheric models to fit H α profiles, and derive the mass accretion rate of the stars and their geometry. In § 4, we discuss the implications of our results. Finally, in § 5 we give our conclusions.

2. TARGETS, OBSERVATIONS, AND DATA SOURCES

In this paper, we work with a subset of the newly identified accretors and possible accretors from Paper I. In general, we include most stars in the Orion OB1 association and stars from other star-forming regions with available archival spectra. Our targets include stars from Chamaeleon I, γ Velorum, σ Ori, Orion OB1, and Upper Scorpius, and they cover a wide range of stellar parameters. We also include two possible accretors, CVSO 1772 and CVSO 1842, in which the He I $\lambda 10830$ lines are in emission without a detectable absorption. Two of our targets, CVSO 1295 and CVSO 1575, are episodic accretors, as their profiles show definite accretion signatures only at some epochs.

2.1. Stellar Parameters

In Table 1, we list the stars included in our survey, their stellar parameters, the type of their He I $\lambda 10830$ profiles, and their rotational properties. We adopted the spectral type, mass, and radius from Paper I. We also gathered the projected rotational velocities $v \sin i$ from

the literature. For some of the stars in which these data are not available, we determined the $v \sin i$ from their spectra (c.f., § 2.3).

2.2. Optical Spectroscopy

We obtained optical spectra of 19 stars out of the 51 new accretors identified in Paper I, using the MIKE spectrograph on the Magellan Clay telescope at the Las Campanas Observatory in Chile. We use the 0.7" slit and the red camera, resulting in the spectral resolution of $R \sim 32500$ for a wavelength range 4900-9500 Å. We reduced the data using the CarPy package (Kelson et al. 2000; Kelson 2003).

In addition to the MIKE data, many of the stars in the southern star-forming regions had been observed using instruments on the ESO/VLT. We downloaded the spectra of these stars from the ESO Archive Science Portal. These data had been reduced and calibrated by their instruments' pipeline. Table 2 shows the details of the observations and data sources.

While the spectral resolutions in these observations are different ($\sim 7 - 16 \text{ km s}^{-1}$), they are sufficient to resolve the H α line; the width of which is of the order of free-fall velocities (\sim few hundreds km s^{-1}). Therefore, we do not expect any significant differences in the line modeling due to the spectral resolution.

2.3. Rotational Velocity

We measured the projected rotational velocities ($v \sin i$) of the stars using the Fourier method, following the procedure of Thanathibodee et al. (2020). We refer the reader to Serna et al. (2021) for a more detailed description of the method employed here. In summary, we corrected the spectra by shifting them with the measured apparent radial velocities calculated using the cross-correlation method with template spectra. We then calculated the Fourier power spectra of at least 3 photospheric lines. The number of photospheric lines used for each star depends on the signal-to-noise ratio of its spectrum and the strength of the absorption lines. The $v \sin i$ were then calculated from the location of the first zero in the power spectra. We include the $v \sin i$ measurement in Table 1, along with the stellar parameters.

3. ANALYSIS & RESULTS

3.1. Mass Accretion Rates and Accretion Geometry

After independently determining that the stars are accreting using the He I $\lambda 10830$ line, we can be certain that the H α emission will have some contribution from the accreting material in the magnetosphere. While it is possible that some stars may be episodic accretors (Paper I) and we did not know if the stars were accreting

Table 1. Adopted and Derived Stellar Parameters of the Targets

Target	Loc	SpT	M_{\star}	R_{\star}	He I ^a	$v \sin i$	Ref. ^b
			(M_{\odot})	(R_{\odot})	$\lambda 10830$	(km s^{-1})	
2MASS J08074647-4711495	γ Vel	M4	0.16	0.84	b	12.9 ± 1.6	(1)
2MASS J08075546-4707460	γ Vel	K3	1.15	1.50	b,br	20.5 ± 4.1	(1)
ISO-ChaI 52	Cha I	M4	0.18	1.17	r	10.46 ± 1.31	(2)
CHSM 13620	Cha I	M2	0.34	1.72	r	18.9 ± 3.5	(1)
SO682	σ Ori	M0.5	0.46	1.83	r	16.58 ± 0.79	(2)
CVSO 40	OriOB1a	M0	0.53	1.47	r	15.23 ± 0.84	(2)
CVSO 156	OriOB1b	M2	0.34	1.96	r	8.71 ± 1.31	(2)
CVSO 298	OriOB1a	M0	0.56	1.33	br	14.56 ± 0.49	(2)
CVSO 1295	Ori Cloud A	K7.5	0.59	1.54	c,r	17.43 ± 1.65	(2)
CVSO 1545	OriOB1b	M4	0.17	1.58	br	9.08 ± 1.35	(2)
CVSO 1575	Ori Cloud A	K7.5	0.57	1.65	c,r	12.60 ± 1.02	(2)
CVSO 1600E	OriOB1b	M3	0.27	1.65	r	15.65 ± 0.54	(2)
CVSO 1600W	OriOB1b	M3	0.27	1.54	r	7.45 ± 3.52	(2)
CVSO 1711	Ori Cloud A	M0	0.52	1.57	r	7.18 ± 2.77	(2)
CVSO 1739	OriOB1b	M5	0.1	1.21	r	14.65 ± 1.62	(2)
CVSO 1763	Ori Cloud A	K3.5	1.09	1.49	r	9.21 ± 2.05	(2)
CVSO 1772 ^c	OriOB1b	M3	0.29	1.04	e	11.79 ± 1.19	(2)
CVSO 1842 ^c	OriOB1b	M2.5	0.32	1.03	e	11.72 ± 2.13	(2)
CVSO 1886	OriOB1b	M3	0.28	1.02	br	17.48 ± 1.07	(2)
CVSO 1928	Ori Cloud A	M0.5	0.47	1.54	r	14.20 ± 0.42	(2)
CVSO 1942	Ori Cloud B	K6	0.72	1.57	r	7.99 ± 2.55	(2)
2MASS J16020757-2257467	USco	M2.5	0.32	1.03	r	14.35	(3)
2MASS J16042165-2130284	USco	K2	1.39	1.98	br	17.30 ± 0.40	(4)
2MASS J16253849-2613540	USco	K7	0.56	2.46	r	17	(5)

^aType of He I $\lambda 10830$ line profile from Paper I: r =redshifted absorption, b =blueshifted absorption, br =blue+redshifted absorption, c =central absorption, and e =emission.

^bReferences for $v \sin i$: (1) Frasca et al. (2015); (2) This study, see § 2.3 for details.; (3) Jönsson et al. 2020; (4) Dahm et al. (2012); (5) James et al. (2006).

^cPossible accretors according to the He I $\lambda 10830$ lines.

during the observation, the targets presented here show telltale signs of accretion in the line profiles, e.g., asymmetric, broad wings or redshifted absorption. These features support the identification with accreting stars.

Given that the procedure and precedence for modeling the H α are well established, and the line modeling is well developed, we used the magnetospheric accretion model to fit the H α lines of the newly identified low accretors to infer the accretion properties of the stars.

3.1.1. Magnetospheric Accretion Model

We used the magnetospheric accretion models of Hartmann et al. (1994) and Muzerolle et al. (1998, 2001), the

details of which are described in the original papers. In essence, the model assumes an axisymmetric accretion flow following a dipolar magnetic field. The flow is described by the disk truncation radius R_i and the width W_r on the disk. The density in the flow is parameterized by the mass accretion rate \dot{M} , whereas the temperature is described by the maximum flow temperature T_{max} . The line profile calculation is done using the ray-by-ray method for a given inclination i .

We created a large grid of models for each star, varying the accretion parameters within ranges appropriate for the observed profile. We started with a large and coarsely spaced grid to search for the approximate loca-

Table 2. Summary of Observations and Data Sources

Target	Instrument	Spectral Resolution	Obs. Date (UT)	Exp. time (sec)	SNR ^a	ESO Program ID
New Observations						
ISO-ChaI 52	MIKE	32500	2020-11-23	2311	30	...
SO682	MIKE	32500	2020-11-23	600	30	...
CVSO 40	MIKE	32500	2020-11-23	803	39	...
CVSO 156	MIKE	32500	2020-11-23	1440	38	...
CVSO 298	MIKE	32500	2020-11-23	1419	40	...
CVSO 1295	MIKE	32500	2020-11-23	900	39	...
CVSO 1545	MIKE	32500	2021-01-17	1200	24	...
CVSO 1575	MIKE	32500	2020-11-23	900	39	...
CVSO 1600E	MIKE	32500	2021-01-17	1200	23	...
CVSO 1600W	MIKE	32500	2021-01-17	600	9	...
CVSO 1711	MIKE	32500	2021-01-17	420	26	...
CVSO 1739	MIKE	32500	2021-01-17	2250	19	...
CVSO 1763	MIKE	32500	2020-11-23	630	36	...
CVSO 1772	MIKE	32500	2021-01-17	1976	12	...
CVSO 1842	MIKE	32500	2021-01-17	1500	16	...
CVSO 1886	MIKE	32500	2021-01-17	1440	16	...
CVSO 1928	MIKE	32500	2020-11-23	720	23	...
CVSO 1942	MIKE	32500	2020-11-23	835	39	...
Archival Data						
2MASS J08074647-4711495 ^b	GIRAFFE	19200	2012-01-01 2012-01-02	6000	34	188.B-3002(A)
2MASS J08075546-4707460 ^b	GIRAFFE	19200	2012-01-03 2012-02-15	2400	147	188.B-3002(A,B)
CHSM 13620	GIRAFFE	19200	2012-04-30	1200	67	188.B-3002(E)
2MASS J16020757-2257467	X-shooter	18340	2019-06-07	1400	95	0103.C-0887(B)
2MASS J16042165-2130284	X-shooter	18340	2019-06-19	520	187	0103.C-0887(B)
2MASS J16253849-2613540	UVES	42310	2005-04-16	780	101	075.C-0272(A)

^aMedian Signal-to-noise of the line and the continuum between 6555-6570 Å.

^bThe spectra for these stars are combined spectra published by the GAIA-ESO survey (Gilmore et al. 2022). They were observed on multiple nights, but the line profiles are similar on both epochs.

tion of the reasonably fit model. For a few representative stars, we started the coarse grid with the range of accretion rates from $10^{-10} M_{\odot} \text{ yr}^{-1}$ to $10^{-9} M_{\odot} \text{ yr}^{-1}$ and T_{max} from 10,000 K to 14,000 K, and inclinations of 10° to 80° . After identifying that the mass accretion rates for the stars were of the order of $1 \times 10^{-10} M_{\odot} \text{ yr}^{-1}$ and $T_{\text{max}} \sim 12,000$ K, we focused our parameter space around these values. After defining a new grid and finding the best fits (c.f., § 3.1.2), we verified that most of the best fits were not at the edge of the parameter space; oth-

erwise, we expanded the parameter space accordingly. Once the approximate parameters were identified, we created the final grid where the parameters are more finely spaced. We adopted the $T_{\text{eff}}=6,000$ K for the accretion shock component on the stellar surface in all cases. This value is less than 8,000 K used for modeling stars at higher accretion rates, as we expected that there is no veiling from the accretion shock in the continuum since it is closer to the effective temperature of the stars. We verified that removing this shock component

Table 3. Range of Model Parameters in the Final Grids

Target	\dot{M} ($10^{-10}M_{\odot} \text{ yr}^{-1}$)	R_i (R_{\star})	W_r (R_{\star})	T_{max} (10^4 K)	i (deg)	a_c	σ_c (km s^{-1})	no.of.models
CVSO 40	1.0/2.0/0.1	2.6/5.0/0.4	0.4/1.6/0.4	1.15/1.25/0.025	10/80/10	0/3.1	0/35	9240
CVSO 156	0.5/2.0/0.1	2.0/5.2/0.4	0.2/2.0/0.2	1.10/1.30/0.025	10/80/10	0/3.1	0/35	103680
CVSO 298	0.5/2.0/0.1	2.0/5.2/0.4	0.2/2.0/0.2	1.10/1.30/0.025	10/80/10	0/2.3	0/35	103680
CVSO 1295	0.5/2.0/0.1	2.0/5.2/0.4	0.2/2.0/0.2	1.10/1.30/0.025	10/80/10	0/1.0	0/35	103680
CVSO 1545	0.5/2.0/0.1	2.0/5.2/0.4	0.2/2.0/0.2	1.10/1.30/0.025	10/80/10	0/7.3	0/35	103680
CVSO 1575	0.5/2.0/0.1	2.0/5.2/0.4	0.2/2.0/0.2	1.10/1.30/0.025	10/80/10	0/1.9	0/35	103680
CVSO 1600E	0.8/3.0/0.2	2.0/5.2/0.4	0.2/2.0/0.2	1.10/1.30/0.025	10/80/10	0/4.2	0/35	77760
CVSO 1600W	0.8/3.0/0.2	2.0/5.2/0.4	0.2/2.0/0.2	1.10/1.30/0.025	10/80/10	0/16.0	0/35	77760
CVSO 1711	0.5/2.0/0.1	2.0/5.2/0.4	0.2/2.0/0.2	1.10/1.30/0.025	10/80/10	0/2.5	0/35	103680
CVSO 1739	0.5/2.0/0.1	2.0/5.2/0.4	0.6/2.2/0.2	1.10/1.30/0.025	10/80/10	0/7.0	0/35	93312
CVSO 1763	0.6/5.0/0.5	2.6/5.0/0.4	0.8/1.6/0.4	1.125/1.25/0.025	10/80/10	0/1.5	0/35	11592
CVSO 1772	0.3/1.5/0.1	2.0/5.2/0.4	0.2/2.0/0.2	1.10/1.30/0.025	10/80/10	0/2.4	0/35	84240
CVSO 1842	0.5/2.0/0.1	2.0/5.2/0.4	0.2/2.0/0.2	1.10/1.30/0.025	10/80/10	0/3.4	0/35	103680
CVSO 1886	1.0/4.0/0.2	1.2/4.4/0.4	0.2/2.0/0.2	1.10/1.30/0.025	10/80/10	0/2.2	0/35	103680
CVSO 1928	0.5/2.0/0.1	2.0/5.2/0.4	0.2/2.0/0.2	1.10/1.30/0.025	10/80/10	0/1.8	0/35	103680
CVSO 1942	0.5/2.0/0.1	2.4/5.6/0.4	0.2/2.0/0.2	1.10/1.30/0.025	10/80/10	0/1.7	0/35	103680
ISO-ChaI 52	0.5/2.0/0.1	2.0/5.2/0.4	0.2/2.0/0.2	1.10/1.30/0.025	10/80/10	0/3.2	0/35	103680
CHSM 13620	0.5/2.0/0.1	2.0/5.2/0.4	0.2/2.0/0.2	1.10/1.30/0.025	10/80/10	0/1.2	0/35	103680
J16020757	0.3/1.5/0.1	2.0/5.2/0.4	0.2/2.0/0.2	1.10/1.30/0.025	10/80/10	0/2.2	0/35	84240
J16253849	0.5/1.5/0.1	2.6/5.0/0.4	0.4/1.6/0.4	1.15/1.25/0.025	10/80/10	0/1.9	0/35	12320
J08074647	0.3/1.5/0.1	2.0/5.2/0.4	0.2/2.0/0.2	1.10/1.30/0.025	10/80/10	0/2.4	0/35	84240
J08075546	0.5/2.0/0.1	2.0/5.2/0.4	0.2/2.0/0.2	1.10/1.30/0.025	10/80/10	0/1.3	0/35	103680
J16042165	0.6/3.0/0.2	2.0/5.2/0.4	0.2/2.0/0.2	1.10/1.30/0.025	10/80/10	0/1.2	0/35	84240
SO682	0.5/1.5/0.1	2.6/5.0/0.4	0.4/1.2/0.4	1.15/1.25/0.025	10/80/10	0/1.3	0/35	9240

(i.e., setting the value to the stellar T_{eff}) had no effect on the overall fitting of the models. Table 3 shows the range of parameters used in the final grid of models for each star. From these grids, we determined the best-fit models and inferred accretion parameters from them.

The reader should be mindful of the limitations of the model when applying the results of this work. In particular, the model assumes no magnetic obliquity and strictly dipolar geometry. Moreover, the temperature distribution in the flow is uncertain. The model that includes magnetic obliquity and non-dipolar fields has not been developed, but simulations with such features exist (Romanova et al. 2003, 2004; Long et al. 2007). However, running such simulations is computationally much more complicated and beyond the scope of this paper.

Some developments have been made to resolve the uncertainty of the temperature distribution in the flow. Using all hydrogen lines observable with the X-shooter

spectrograph, Colmenares et al. (in prep.) found that the temperature distribution assumed in our model is consistent with a large number of stars in the Lupus and Chamaeleon I region. Specifically, the hydrogen line decrements (c.f., Antonucci et al. 2017) found in the observations are mostly consistent with that calculated from the same model we used here. Therefore, we argue that the uncertain nature of the temperature distribution would not be a major effect in our analysis.

3.1.2. Fitting the Line Profiles

To fit the model to observation, we first removed the photospheric absorption lines from the observed spectrum using a PHOENIX model spectrum (Husser et al. 2013) with an appropriate effective temperature and gravity for the star. That is

$$F_{\text{obs}} = F_{\text{obs},0} - F_{\text{phoenix}}(T_{\text{eff}}, \log g) + 1, \quad (1)$$

where F_{phoenix} has already been convolved to the spectral resolution of the observation, and all the spectra involved are normalized to unity.

Previous studies show that the chromospheric contribution to the $\text{H}\alpha$ line can be significant in low accretors (Manara et al. 2017a), and line profile modeling has to take the chromospheric emission into account. In our previous study (Thanathibodee et al. 2020), we approached this problem by fitting the residual between the best fit model profiles and the observation with a Gaussian and found that a Gaussian function can fit the residual qualitatively well. This was expected since chromospheric lines, being formed approximately uniformly on the stellar surface, are narrow and symmetric (e.g. Batalha et al. 1996). Since we do not attempt to fit the stars' actual chromosphere, a Gaussian function is sufficient for our purpose. In this paper, we account for the chromospheric contribution by directly incorporating the Gaussian into the fitting procedure.

For each model line flux in the velocity space $F_v(\dot{M}, R_i, W_r, T_{\text{max}}, i)$, the total model is given by

$$F_{v,\text{total}} = F_v(\dot{M}, R_i, W_r, T_{\text{max}}, i) + a_c e^{-v^2/(2\sigma_c^2)}, \quad (2)$$

where a_c and σ_c are the amplitude and the width of the Gaussian function representing the chromosphere in the unit of the continuum and km s^{-1} , respectively. Here we fixed the center of the Gaussian at the stellar rest velocity. We then calculated the fit statistics by varying a_c and σ_c to minimize the χ^2 ,

$$\chi^2 = \sum_j \frac{(F_{j,\text{total}}(a_c, \sigma_c) - F_{j,\text{obs}})^2}{F_{j,\text{obs}}}, \quad (3)$$

where j indexes over the pixels within $\pm v_{\text{ff},\infty} = \sqrt{2GM_\star/R_\star}$, the free-fall velocity from infinity, and F_{obs} is the normalized observed flux in the native spectral pixels.

To determine the best fit model in a given grid, we calculated the likelihood,

$$L = N e^{-\chi^2/2}, \quad (4)$$

for each combination of model parameters. $N = e^{\chi_0^2/2}$ is a normalization chosen so that the highest likelihood in the grid is unity and χ_0^2 is the lowest χ^2 in a given grid.

Figure 1 shows the examples of the best fits for two stars employing our fitting procedures. The line profile of CVSO 1928, shown on the left panel of the figure, shows a redshifted absorption component and a slightly broader blue wing compared to the red. In this case, the chromosphere contributes significantly to the line profile, accounting for most of the emission at the line center, whereas the magnetosphere contributes mostly to the wing. On the other hand, the magnetospheric contribution can account for most of the line profile

of CVSO 1295, shown on the right panel of Figure 1. The magnetospheric model can simultaneously fit the low-velocity redshifted absorption and wide blue and red wings. Extra redshifted absorption in CVSO 1886 and J16042165 are not accounted for, but, as discussed earlier, their contributions to the overall profiles are small. The accretion flows that cause such features are expected to have much lower accretion rates than the main accretion flows producing the emission profiles (Thanathibodee et al. 2019).

Some residual can also be seen near the peak, where the model slightly under-predicts the emission. This could be where the chromospheric emission can contribute. However, in our approach, we assume that the model components are additive, which may not be the case for lines where the magnetospheric flow absorbs light from both the photosphere and the chromosphere. A possible approach to account for such radiative transfer effect is to include a Gaussian component as a proxy for the chromosphere, in addition to the continuum/photosphere from the star, in the profile calculations. However, such an approach is much more computationally expensive than we have adopted here, especially when many stars are involved. Another approach is to fix the chromospheric line *a priori* from independent measurements; this requires knowledge of the formation of chromospheric emission lines. These approaches will be explored in future studies. In any case, the residual is only a few percent of the line peak and should not contribute significantly to the determination of accretion properties.

3.1.3. Inferring the Accretion Parameters

For each star, we determined the accretion parameters by calculating the weighted mean and standard deviation of each parameter from models with a normalized likelihood of more than 0.5, where we used the likelihood L as the weight. Table 4 shows the accretion parameters retrieved from the magnetospheric accretion modeling and Figure 2 shows the $\text{H}\alpha$ profiles where the accretion models can fit the observation qualitatively well. We also list the lowest χ^2 for a given star in Table 4. The low values of χ_0^2 also confirm that the accretion models fit well. We plot the distribution of the parameters for all the samples selected for analysis in Figure 3.

3.1.4. Stars Excluded from Further Analysis

As shown in Figure 4, the magnetospheric accretion model has difficulty reproducing observations of four stars. All of these stars show low-velocity redshifted absorption features in the line profile, but the magnetospheric model cannot reproduce the absorption feature while producing enough emission to fit the emission component of the line. This is unlike the case of CVSO 1295 (Fig. 1), in which the emission component

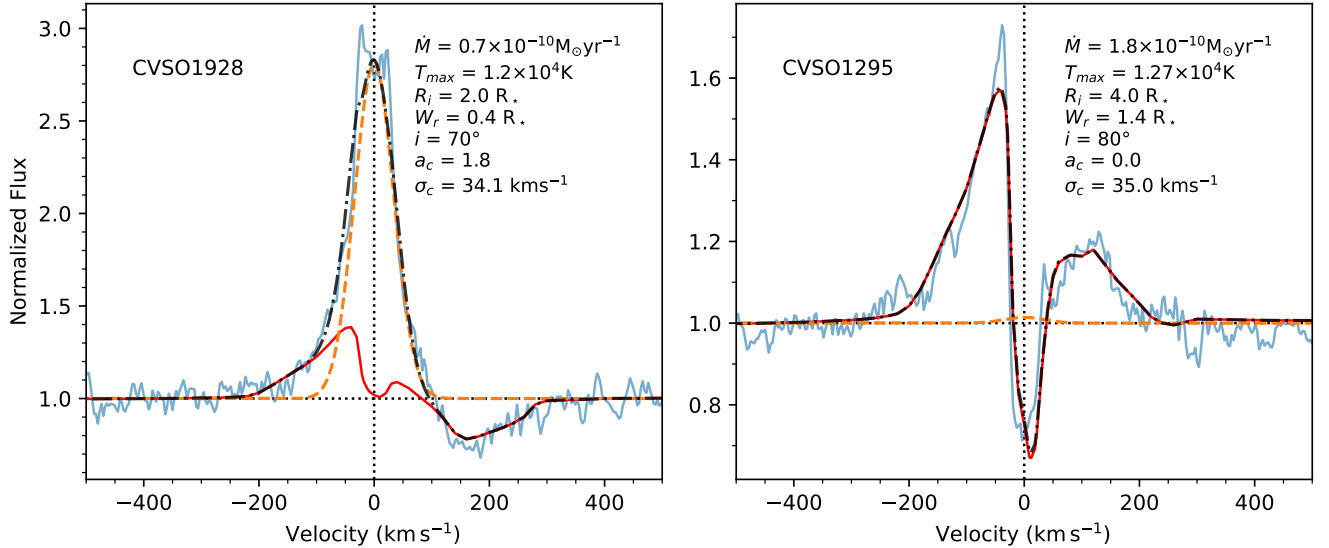


Figure 1. Examples of the fitting procedure incorporating the chromospheric emission. The dotted horizontal and vertical lines show the continuum level and the line center, respectively. The solid blue lines are the observation. The solid red lines are the contribution from the magnetospheric model. The dashed orange lines are the best fits for the chromospheric components of the line. The dash-dotted black lines are the best fit total model.

is weak, ~ 1.5 times the continuum, while in these stars the line peaks at $\sim 2.5 - 5$ times the continuum. We speculate that these stars have a flow structure similar to the low accretor CVSO 1335, with its conspicuous low-velocity redshifted absorption in the $H\alpha$ line in multi-epoch observations (Thanathibodee et al. 2019). Modeling these lines would likely require the two-flow models, as for CVSO 1335. In the interest of comparing the parameters for large numbers of low accretors, as opposed to performing a detailed study of individual objects, we exclude these four stars from further analysis.

4. DISCUSSION

In this section, we discuss inferences that can be drawn from the accretion rates and flow geometries determined for the sample of low accretors. As explained above, we exclude four stars that seem to require more complex geometries to fit their $H\alpha$ profiles (Thanathibodee et al. 2019). Therefore, the discussion in this section will be based on 20 stars, indicated as ‘Y’ in Table 4.

4.1. Accretion Rates and Stellar Properties

Simulations of accreting magnetized stars have shown that accretion occurs differently depending on the geometry of the magnetic field. Analytical arguments, assuming a dipolar magnetic field, relate the accretion properties and those of the star with the expression

$$R_M = \xi \left(\frac{\mu^4}{4GM_*\dot{M}^2} \right)^{1/7} \approx 18\xi \frac{B_3^{4/7} R_2^{12/7}}{M_{0.5}^{1/7} \dot{M}_{-8}^{2/7}}, \quad (5)$$

where R_M is the magnetic radius, at which the field truncates the disk, μ is the magnetic moment, B_3 is

the strength of the surface dipolar magnetic field in kG, $R_2 = R_*/2R_\odot$, $M_{0.5} = M_*/0.5M_\odot$, \dot{M}_{-8} is the mass accretion rate in the unit of $10^{-8} M_\odot \text{ yr}^{-1}$, and ξ encapsulates the details of the disk-magnetosphere interaction (Hartmann et al. 2016). From this equation, we expect that the geometry of the accretion flow, represented by the magnetic radius, will depend on the mass accretion rates for similar stellar parameters.

Mass accretion depends on the rotational velocity of the star. One metric used to determine if the system is in the accreting regime or in the propeller regime when accretion does not occur is the fastness parameter, defined as a ratio between the angular velocity of the star and the angular Keplerian velocity at the magnetic radius. It can be written as (e.g., Ghosh & Lamb 1979; Romanova et al. 2018)

$$\omega_s = \frac{\Omega_*}{\Omega_K(R_M)} = \left(\frac{R_M}{R_{co}} \right)^{3/2}, \quad (6)$$

where Ω_* is the angular rotational velocity, $\Omega_K(R_M)$ is the angular Keplerian velocity at R_M , and R_{co} is the corotation radius.

In this sub-section, we investigate these relationships to determine the properties of the low accretors.

4.1.1. Accretion Rates and Accretion Geometry

In the left panel of Figure 5, we plot the truncation radius R_i versus the mass accretion rates. Due to the relatively large uncertainty in both parameters, we adopted the orthogonal distance regression (ODR; Boggs et al. 1987) to determine the trend between the parameters, as opposed to the simple linear regression. This method

Table 4. Results of the Magnetospheric Accretion Model

Star	\dot{M} ($10^{-10} M_{\odot} \text{ yr}^{-1}$)	R_i (R_{\star})	W_r (R_{\star})	T_{max} (10^4 K)	i (deg)	a_c ^a	σ_c (km s^{-1})	χ_0^2	Good
CVSO 40 ^b	2.0±0.0	4.2±0	1.2±0	1.23±0.0	80±0	0.0±0	35.0±0	50.33	N
CVSO 156	1.4±0.4	2.6±0.7	0.7±0.3	1.2±0.06	79±3	2.7±0.4	25.7±2.7	1.97	Y
CVSO 298	1.3±0.5	4.3±0.9	0.9±0.4	1.19±0.06	78±6	2.2±0.3	26.9±3.7	0.77	Y
CVSO 1295	1.5±0.4	4.4±0.6	1.1±0.4	1.22±0.06	79±0	0.1±0.1	24.6±15.5	0.81	Y
CVSO 1545	1.4±0.4	2.7±0.9	0.9±0.5	1.21±0.06	74±7	4.0±2.3	33.1±6.5	2.21	Y
CVSO 1575	1.0±0.2	2.0±0.1	0.2±0.0	1.18±0.06	80±0	0.6±0.2	14.6±9.0	3.78	Y
CVSO 1600E	2.3±0.5	2.5±0.6	1.0±0.4	1.18±0.06	80±0	3.5±0.5	25.6±2.3	2.61	Y
CVSO 1600W	2.8±0.3	2.9±0.2	1.5±0.2	1.24±0.05	40±0	4.1±1.3	30.4±4.9	9.52	Y
CVSO 1711	1.2±0.5	3.5±1.2	0.6±0.4	1.2±0.06	79±3	2.3±0.3	30.7±3.4	0.79	Y
CVSO 1739	1.7±0.2	2.4±0.1	1.8±0.2	1.22±0.04	80±0	3.1±0.5	21.6±1.5	4.28	Y
CVSO 1763	3.8±0.6	3.6±0.5	1.2±0.0	1.21±0.03	79±0	0.0±0.0	4.4±11.6	9.84	N
CVSO 1772	0.4±0.1	4.1±1.2	0.5±0.2	1.14±0.05	80±0	2.4±0.1	24.3±1.6	3.6	Y
CVSO 1842	1.0±0.4	4.3±0.9	0.9±0.4	1.11±0.02	80±0	3.3±0.1	22.1±1.2	8.32	Y
CVSO 1886	2.9±0.8	1.9±0.3	1.9±0.1	1.27±0.03	80±0	1.5±0.1	25.5±2.5	2.42	Y
CVSO 1928	1.3±0.4	3.6±1.1	1.2±0.5	1.2±0.06	32±17	1.5±0.3	32.2±4.1	1.13	Y
CVSO 1942	1.3±0.4	3.5±1.0	0.7±0.3	1.21±0.06	36±16	1.2±0.3	30.2±5.4	0.88	Y
ISO-ChaI 52	1.1±0.4	4.1±0.8	1.4±0.5	1.15±0.05	80±0	2.1±0.4	23.0±2.8	1.59	Y
CHSM 13620	1.4±0.4	2.6±0.4	0.9±0.3	1.22±0.06	79±1	0.7±0.2	22.5±4.6	0.82	Y
J16020757	0.7±0.3	3.7±0.9	1.3±0.5	1.18±0.06	35±23	2.1±0.2	30.6±5.1	0.36	Y
J16253849	1.1±0.2	2.7±0.2	0.4±0.0	1.21±0.05	79±0	0.0±0.0	0.2±0.3	136.69	N
J08074647	0.4±0.1	2.7±0.6	0.7±0.2	1.15±0.05	76±11	2.4±0.0	25.0±1.8	2.41	Y
J08075546	1.4±0.4	3.2±0.8	0.5±0.2	1.22±0.06	42±8	0.5±0.1	26.7±8.4	0.67	Y
J16042165	2.1±0.7	4.0±0.9	0.5±0.2	1.23±0.06	66±5	0.5±0.2	22.2±10.5	0.41	Y
SO682	1.3±0.2	3.6±0.5	0.9±0.2	1.22±0.03	80±0	0.0±0.0	3.7±5.0	13.92	N

^a a_c is in units of the continuum level as the profiles are fitted to the normalized flux.

^bToo few models to determine uncertainty.

takes into account the uncertainty in both parameters in calculating the regression and its associated uncertainty. The black dashed line shows the fit for the overall sample, suggesting that the truncation radius increases as the mass accretion rate decreases.

The characteristics of the magnetic fields in T Tauri stars depend on the properties of the stars on their evolutionary tracks (e.g., Villebrun et al. 2019); the magnetic field strength becomes weaker as stars evolve from being fully convective to having radiative cores, for example. This evolution depends on the stellar mass and the age, which are reflected in the spectral type. In general, earlier spectral type (K-type) T Tauri stars are more massive and/or older than later type T Tauri stars. On the left panel of Figure 5, we separate the K-type stars from the M-type stars. For the K-type stars, the

truncation radii tend to be high, $\sim 4 R_{\star}$, regardless of the mass accretion rate. Kendall's tau correlation test with $p=0.23$ suggests that the two parameters are uncorrelated for K stars. However, this result is based on a small sample size and a larger sample is needed to verify it.

On the other hand, for the M-type stars, there is a more significant correlation between the two parameters (Kendall $p=0.006$) than for the whole sample (Kendall $p=0.07$). This trend for the M-type stars is expected from the relationship presented in Eq. 5, suggesting that dipolar magnetic fields still dominate the accretion processes in low-mass low accretors. The same cannot be said for higher mass stars, as no obvious trend emerges. It is possible that as the star gets older (for their masses), the dipolar magnetic fields become

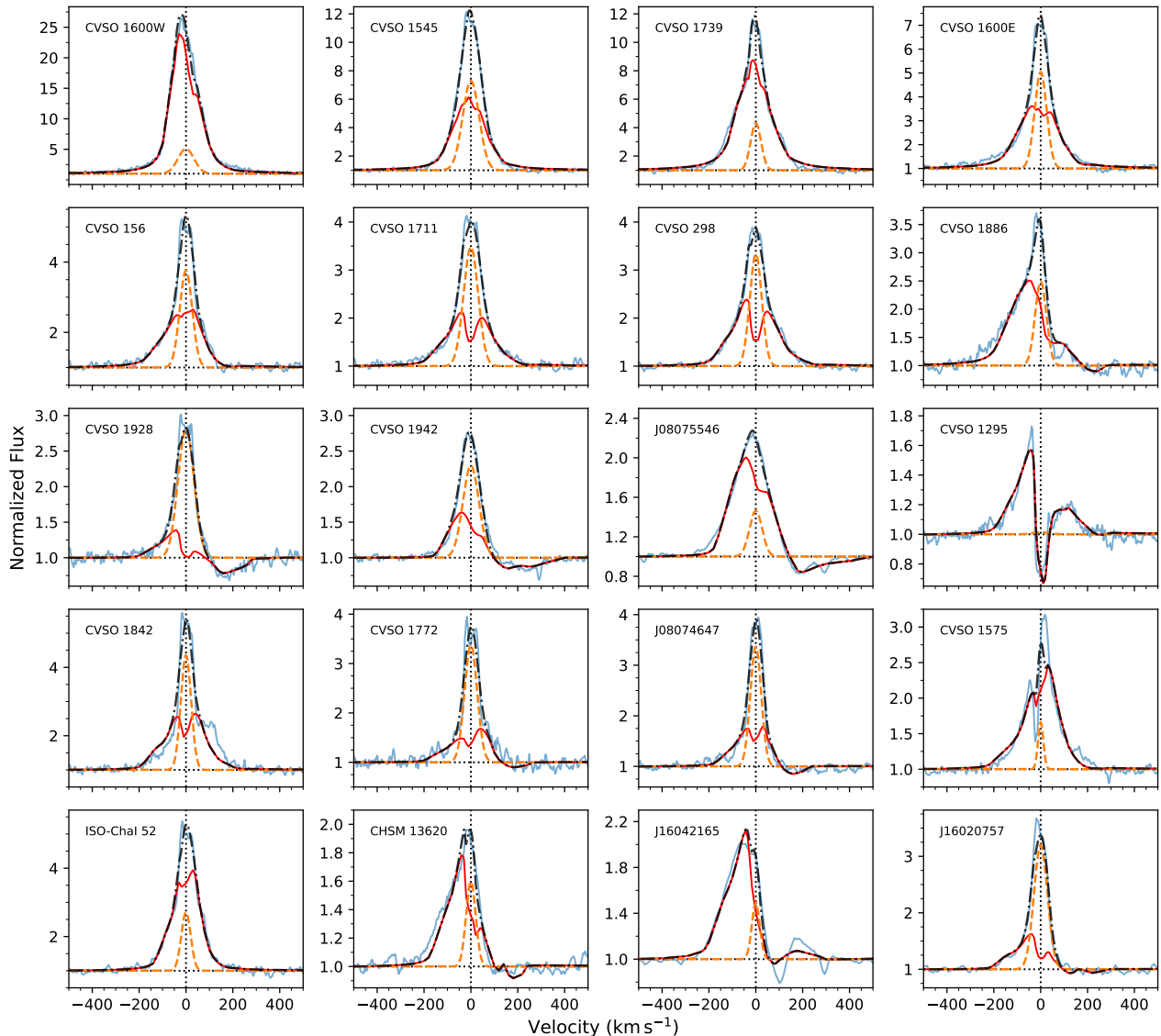


Figure 2. The best fits H α line modeling for stars with good fits. Line types and colors as in Figure 1.

weaker, as expected in studies directly measuring magnetic field properties of T Tauri stars (Villebrun et al. 2019; Lavail et al. 2017), making the relationship between R_i and \dot{M} less meaningful as it is derived from an assumption of dipolar field.

Fitting a linear relationship with ODR to the M-type stars, we found that the mass accretion rates and the truncation radius are related by a power law given by

$$R_i \propto 1/\dot{M}^{0.30 \pm 0.12}. \quad (7)$$

This result is robust against the star with the low accretion rates and small R_i in our sample (J08074647, $\log \dot{M} = -10.40$), without which we have the exponent of 0.41 ± 0.14 .

The exponent (0.30 ± 0.12) is consistent with that found by simulations (0.19-0.22, Blinova et al. 2016; 0.2, Kulkarni & Romanova 2013; 0.34, Ireland et al. 2021),

or that derived from equating the disk ram pressure and the magnetic pressure, as in Eq. 5, $2/7 = 0.29$. This suggests that in M stars, the assumption of dipolar geometry of the accretion flows is still valid.

4.1.2. Accretion Geometry and Rotation Properties

It is known from theoretical studies and simulations that accretion can be in different regimes depending on the relationship between the corotation radius and the disk truncation radius. The fastness parameter ω_s , relating the truncation radius and the corotation radius (Eq. 6), can be used to classify accreting into different regimes. The system is in the propeller regime if $\omega_s > 1$ ($R_i > R_{co}$), and steady accretion cannot occur. Instead, some mass will get ejected from the system through winds, while some mass accumulates at the transition region between the two radii and gets periodically loaded

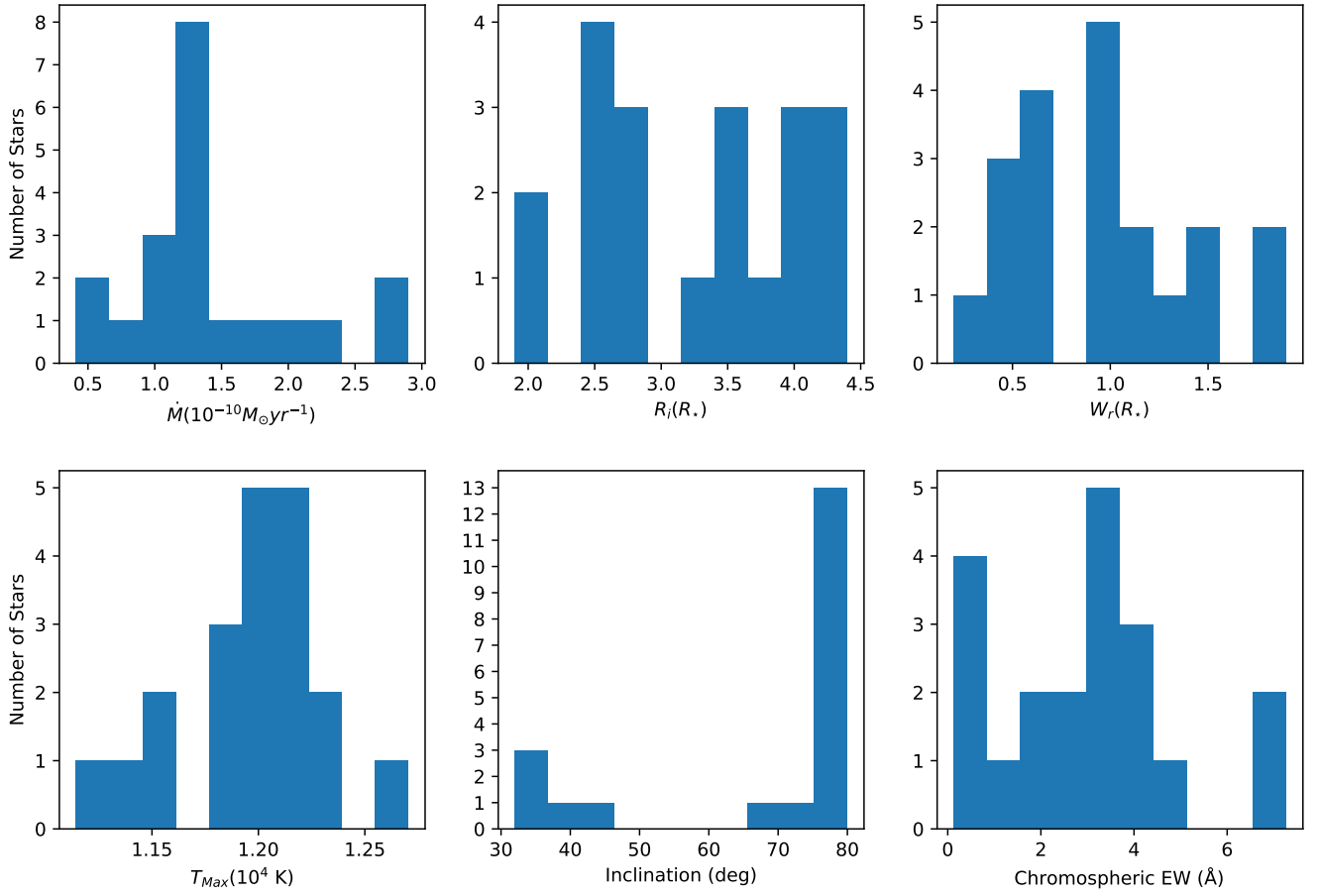


Figure 3. The distribution of model parameters for the 20 stars included in the analysis.

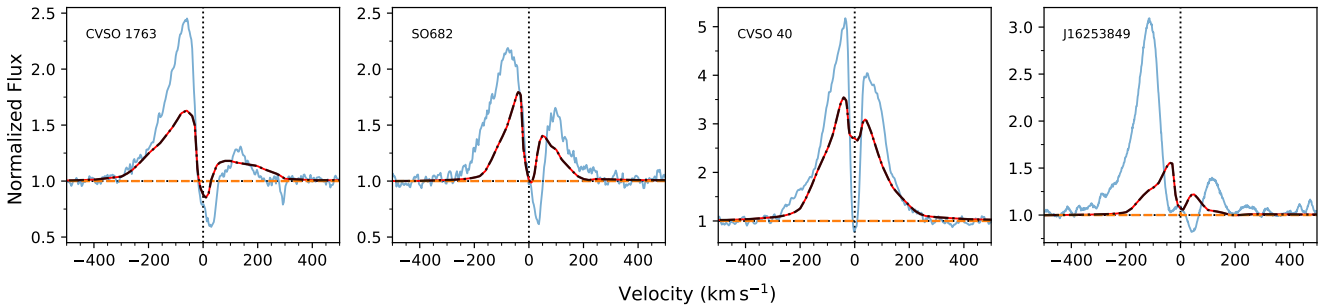


Figure 4. Same as Fig. 2, but for stars where the accretion flow model has difficulties reproducing the observations.

onto the star (e.g., Romanova et al. 2018). For non-propellers, accretion may be in a stable or an unstable regime. In the stable regime, accretion occurs in large funnels and the light curve of the star, modulated by accretion hot spots, will be periodic (Romanova et al. 2008). Our axisymmetric accretion flow models most resemble these types of flows. The unstable regime, in turn, can be classified into two types based on how the mass is loaded onto the star. In the chaotic unstable regime, mass is loaded in several tongues that could be short-lived, whereas the ordered unstable regime is char-

acterized by tongues merging to form one to two funnels (Blinova et al. 2016).

The boundaries between these regimes also depend on the magnetic obliquity, i.e., the misalignment between the rotation axis and the magnetic axis. Accretion is in the ordered unstable regime for $\omega_s \lesssim 0.45$ for a wide range of the values of obliquity, and the boundary between the stable and unstable regime is $\omega_s \sim 0.54 - 0.6$ for a misalignment between 5° and 20° (Blinova et al. 2016).

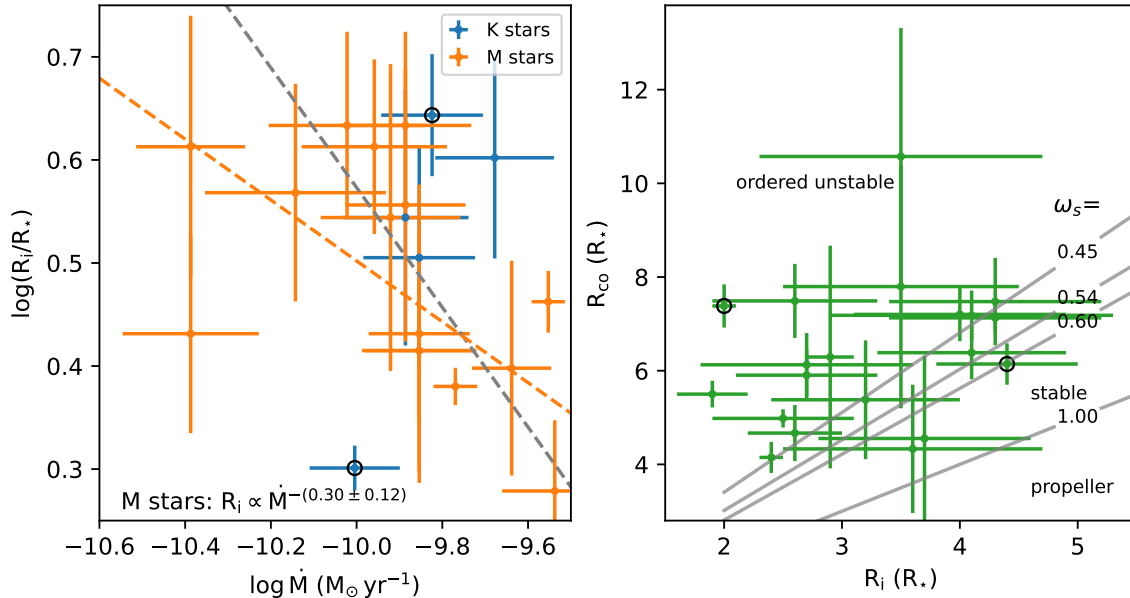


Figure 5. Relationships between the truncation radius R_i and the mass accretion rate and the corotation radius in low accretors. *Left:* The truncation radius as a function of \dot{M} , plotted in log scale. K-type stars are plotted in blue and M-type stars are plotted in orange. The gray line is the best fit calculated from linear orthogonal distance regression for the whole sample. The orange line is the fit for M-type stars. *Right:* The corotation radius as a function of the truncation radius. The gray lines correspond to different radius ratio for different values of fastness parameters ω_s , shown on the plot. The lower right region of the plot is the propeller regime and the upper left region is the ordered unstable regime. The boundary between the stable and unstable regime is $\omega_s \sim 0.54 - 0.6$, depending on the obliquity of the magnetic axis (Romanova et al. 2008, 2018). Stars marked in black circles are episodic accretors.

The corotation radius is typically calculated from the rotation period of the star and the known mass and radius. Since the rotation periods of most of the stars in our sample are not available, we have to infer the period from the projected rotational velocity $v \sin i$. Assuming that the inclination of the stellar rotation is the same as the inclination found from the line modeling (Table 4), we calculated the corotation radius as

$$R_{co} = \left[\frac{GM_* R_*^2 \sin^2 i}{(v \sin i)^2} \right]^{1/3}. \quad (8)$$

Since the assumption of axial symmetry is not necessarily correct, we adopted a minimum uncertainty of 15° for the inclination unless the modeling results suggest a larger value. The uncertainties in the final values are calculated using standard error propagation methods.

The right panel of Figure 5 shows the relationship between the truncation radius and the corotation radius. Four solid lines show the boundary between accretion regimes based on the value of the fastness parameter. None of our targets is in the propeller regime, including the possible accretors (CVSO 1772, CVSO 1842) and episodic accretors (CVSO 1295, CVSO 1575) in our sample. A likely explanation is that these stars are accreting most of the time, but the accretion detection using He I $\lambda 10830$ in Paper I has some limitations, as discussed therein.

Most of the targets are in the unstable regime, with about half of them in the ordered unstable regime. Given that the gap between the ordered unstable regime and the stable regime is small, it is likely that most of our targets are in the regime in which large funnel flows are present, and applying the magnetospheric model to these cases is appropriate.

These results suggest that low accretors, except for having large truncation radii, are accreting “normally” and they are not close to the propeller regime. As noted above, this interpretation is dependent on the assumption that there is no magnetic obliquity. In reality, corotation radii calculated from Eq. 8 are likely to be upper limits, as the mean inclination should be $\sim 60^\circ$. Nevertheless, the R_{co} depends on $\sin^{2/3}(i)$, so the effect of inclination is small at a moderate to high inclination. Therefore, there could be more stars in the stable regime, but it is unlikely that any stars would be in the propeller regime. In addition, the assumption that stars accrete via dipolar fields may influence the interpretation of the results in the accreting regime (however, see Section 4.1.3), but the geometry of the magnetic field should not affect the boundary between accreting and propeller regime.

While the exact region on which a particular star is accreting may be uncertain, we can infer that accretion stops not because the system reaches the propeller

regime but from other processes. However, another possibility is that our samples do not include stars nearing the propeller regime because they were not identified as accretors even with the He I $\lambda 10830$ line. Testing this hypothesis would require observing stars identified as possible accretors in multi-epoch observations.

4.1.3. *The Disk-Magnetosphere Interaction of Low Accretors*

Equation 5 provides an explicit relationship between accretion rates and accretion and stellar properties, as discussed above. Given that $R_M = R_i$, the truncation radius, we can use the measurements from our sample to determine the average values of the magnetic field B and the efficiency parameter ξ .

Figure 6 shows the relationship between the truncation radius R_i inferred from the magnetospheric accretion flow model fitted to observations and the magnetic radius R_M calculated from Eq. 5 using the inferred \dot{M} . Different colors in the plot refer to different strengths of the surface dipolar magnetic field.

The dashed lines are the best linear fits calculated using the orthogonal distance regression, as in Figure 5, and the solid gray lines are the one-to-one relationship. While R_i and R_M show weak correlation, with Kendall $\rho=0.07$, it is suggestive, from these fits, that for the magnetic radius to be the same as the truncation radius, the stars generally require a low value of ξ or a low value of the magnetic field B .

We can compare these values to that of theoretical expectation ($\xi \sim 1$), and numerical simulations. For example, Kulkarni & Romanova (2013) and Blinova et al. (2016), using the large suites of models of their numerical simulations, investigated the relationship between the magnetic radius calculated from the models and that calculated from theoretical prediction such as that presented in Eq. 5. Their models are for truncation radii between $\sim 2 - 6 R_*$, which are appropriate for comparison with our data. Blinova et al. (2016) found that the parameter ξ ranges from $0.5 \lesssim \xi \lesssim 0.9$ for stable accretion and $0.8 \lesssim \xi \lesssim 0.93$ for unstable accretion; a similar range is found by Kulkarni & Romanova (2013).

For our estimates to be consistent with the high values of ξ obtained in the simulations, the magnetic field strength needs to be as low as 0.1 kG or even lower, as the analysis in Figure 6 indicates. Given that the total magnetic field strength in T Tauri stars is on the order of a few kG (e.g., Lavail et al. 2019), this suggests that the magnetic field that is responsible for accreting mass, i.e. the dipolar field, is very weak compared to other topologies (e.g., quadrupole and octupole). Weaker dipole components compared to higher order fields are found in observations (e.g., Gregory et al. 2008; Donati et al. 2011; Chen & Johns-Krull 2013), but not as much as that of our results. It is possible that as the star evolves, most of the magnetic field lines are in the higher order configuration, but we can still see accretion as if the

dipolar field dominated because the mass accretion rate is so low such that even a weak field is able to truncate the disk. To test this hypothesis, measurements of the components of the magnetic fields in very low accretors would be required.

We also note that the simulations suggesting high values of ξ are run for stars accreting at relatively high accretion rates, $\sim 10^{-7} M_\odot \text{ yr}^{-1}$. It is possible that at low accretion rates, the efficiency for the magnetic fields to truncate the disk decrease significantly. Whether the two parameters are directly related, or they result from a common cause (e.g., the evolution of stars/disks) is unclear. Simulations of accreting stars at very low rates are needed to explore this scenario.

4.2. *The Distribution of Accretion Parameters*

To search for common properties among the low accretors, we plot the distributions of the best fit model parameters for the 20 stars in Figure 3. The mass accretion rates and the truncation radii are discussed separately in §4.1 and §4.4. Here, we discuss the findings and implications for other parameters.

4.2.1. *Inclination*

Perhaps the most surprising finding in these distributions is that the inclinations of low accretors are very high. It is possible that this is in part due to the assumption that there is no magnetic obliquity, and the inclinations of the stellar rotation axes are somewhat smaller than $\sim 80^\circ$. Tilted magnetospheres should produce light curves that are different from aligned magnetospheres (e.g., Romanova et al. 2004). Photometric monitoring of these stars will help to test this hypothesis.

Another possibility for the high inclinations is that it is an observational bias in the survey to search for low accretors (Paper I), which used the equivalent width and the width at 10% peak (W_{10}) as criteria for selecting low accretor candidates.

We illustrate this bias in Figure 7, in which we show $H\alpha$ profiles calculated for an M2 low accretor observed at different inclinations. The spectral type of the star is the median spectral type of the newly identified accretors in Paper I. We assumed that the chromospheric contribution to the line, modeled as a Gaussian, stays constant at $EW=4.1 \text{ \AA}$, i.e., more than 50% lower than White & Basri (2003)'s threshold of accretion for an M2 star. As shown by panel (a) of the Figure, the line profiles change both in strength and shape as the viewing inclination changes. In particular, at a low inclination, the total line profile (shown in blue) is dominated by the emission from the magnetosphere. The line is also brighter since few regions of the flow are occulted by the star, the flows in front, or the disk. However, the line is narrow at low inclinations, as the line of sight is closer to normal with the poloidal velocity field of the accretion flow. The line becomes weaker and broader

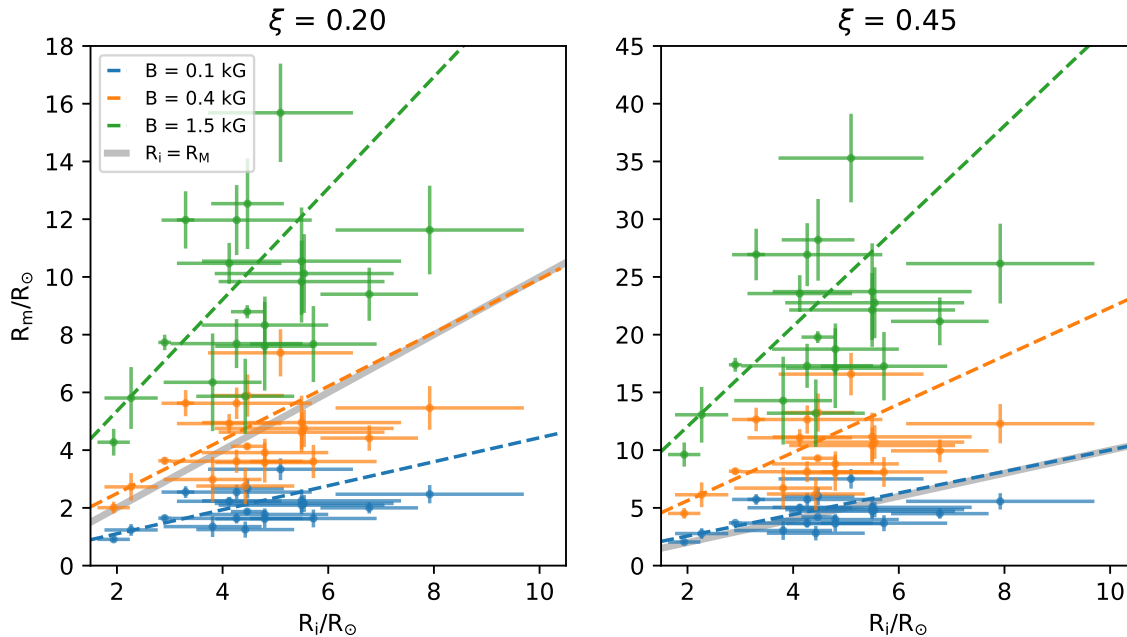


Figure 6. The magnetic radii calculated from mass accretion rates and the inferred truncation radii from the model, varying ξ and the surface magnetic field strength B . Different colors refer to different magnetic field strengths. The dashed lines are the linear regressions of the two radii. The solid gray lines are the one-to-one relationship between the two measurements.

at high inclinations, due to the same effects discussed above. In this limit, the chromosphere dominates the emission line.

When observations are made to determine accretion status, no chromospheric contribution is removed, as it is unknown. Therefore, the measurement of EW and W_{10} will intrinsically include the effect of the chromosphere. Panel (b) of Figure 7 shows the measurement of EW and W_{10} for the profiles in panel (a) with and without the chromospheric contribution. For reference, the thresholds for accretion classification, $EW \geq 10 \text{ \AA}$ and $W_{10} \geq 270 \text{ km s}^{-1}$ (White & Basri 2003), are indicated in the Figure. Without the chromospheric contribution, the star would have been classified as accretor if the EW criterion had been used, and if it had an inclination of 45° or less; at higher inclinations, the EW would be below, or at least barely above, the threshold. On the other hand, it would be classified as an accretor at high inclination if the W_{10} criterion had been used.

Taking into account the chromosphere, a similar trend is found for equivalent widths, except that it would need to have a high inclination, $\geq 60^\circ$, to be classified as a non-accretor. For W_{10} , it would always be classified as a non-accretor, regardless of inclination. This is because, at a high inclination, the peak is raised by the chromospheric contribution, so the measurement at the 10% peak is at the narrower part of the line profile.

In Paper I, stars selected as low accretor candidates are those classified as non-accretors using either W_{10} or EW . Since most of the targets were selected based on the equivalent width of $H\alpha$, the survey preferentially

includes stars at higher inclination as those are stars with the highest chance of being (mis)classified as non-accretors. Therefore, it is not surprising that most of our targets show high inclinations in magnetospheric modeling.

While the above explanations are applicable to cases with high inclinations, there are still some stars in our sample with low inclinations, but none have moderate inclinations. There are five stars with fitted inclinations of less than 45° , including CVSO 1600W, CVSO 1928, CVSO 1942, J16020757, and J08075546. As shown in Figure 2, the best fits for most of these stars (except CVSO 1600W) show that the $H\alpha$ line profiles are dominated by chromospheric emissions with subtle broad wings. It could be that at a low inclination, more of the chromosphere could be seen as it is not occulted by the magnetospheric flows. Therefore, with low accretion rates and low inclinations, the signatures of accretion in the $H\alpha$ line can be hard to detect, and there is a chance that the accretion status can be misclassified compared to accretors observed at moderate inclinations.

Lastly, the derived high inclinations in our analysis could be due to other unaccounted factors in the modeling. To quantify these effects, a comparison between the inclination derived from the modeling and those calculated from rotation periods will be needed. However, the rotation periods of most of the samples are not available, and deriving periods from light curves would be outside the scope of this paper. Nevertheless, we can qualitatively estimate how likely it is for the samples to have high inclinations. For a star with $R = 1.5R_\odot$ (a typical

value for our sample) and a period of 5.84 days (a typical value for WTTS in Orion OB1; Karim et al. 2016), we get $v \sin i \sim 13 \text{ km s}^{-1}$ for $i = 90^\circ$. An accreting system is expected to have a longer period and hence even lower $v \sin i$. Therefore, the measure $v \sin i$ of our samples ($\sim 7 - 20 \text{ km s}^{-1}$) are not inconsistent with high inclinations found in the modelings.

4.2.2. The Equivalent Width of the Chromospheric Emission

For the parameters related to the Gaussian chromospheric contribution, we plot instead the equivalent width of the chromospheric line, calculated as

$$EW_c = \sqrt{2\pi} a_c \sigma_{c,\lambda}, \quad (9)$$

where $\sigma_{c,\lambda}$ is the Gaussian width converted to wavelength scale.

As shown in the last panel of Figure 3, most of the stars have the EW of the chromospheric component less than 5 \AA , and a portion of them require very small or almost no chromospheric contribution. We compared the EW of the chromospheric emission to that of the observation and found that, on average, the chromospheric emissions account for $\sim 30\%$ of the overall profile. For three targets (CVSO 1928, J16020757, J08074647), the chromospheric emission can be up to $\sim 60\%$ of the line. These results confirm previous findings that the chromospheric contribution can be very significant in the line (e.g., Manara et al. 2013).

4.3. The Lowest Measurable Mass Accretion Rates

The distribution of mass accretion rates of our sample, shown in Figure 3, suggests that most of the stars accrete at $\sim 10^{-10} \text{ M}_\odot \text{ yr}^{-1}$, with the lowest at $\sim 5 \times 10^{-11} \text{ M}_\odot \text{ yr}^{-1}$. Is this a physical limit, or is it the lowest rate that can be measured using line modeling?

To address this question, we ran two grids of models for two 5 Myr stars, a K5 star and an M3 star, accreting at very low accretion rates, from $10^{-12} \text{ M}_\odot \text{ yr}^{-1}$ to $10^{-10} \text{ M}_\odot \text{ yr}^{-1}$. The two spectral types are representative of the targets in our sample. As the line profiles also depend on the geometry and temperature, we also varied R_i , W_r , and T_{max} within the ranges found in Figure 3. We fixed the inclination at 60° . In all cases, we assumed no contribution from the accretion shock. For each case, we include a contribution from the chromosphere with a Gaussian. We adopted the amplitude $a_c = 1$ for K5, $a_c = 3$ for M3, and $\sigma_c = 25 \text{ km s}^{-1}$ for all spectral types. These values are consistent with the results in Table 4.

We show the results of the two small grids in Figure 8. In both stars, the emission component is stronger for large and narrow magnetospheres, as in Muzerolle et al. (2001). The redshifted absorption component of the line can be seen in all geometries for wide ranges of accretion rates. Assuming that we can detect a feature in the line that has $\sim 30\%$ deviation from the continuum (i.e., signal-to-noise ~ 3 , see also CVSO 1928

in Fig. 2), we can estimate the lowest mass accretion rates detectable with each model by determining if the broad wings in emission is greater than ~ 1.3 and the absorption feature is deeper than ~ 0.7 , both in the normalized unit of the continuum. For the K5 stars, we can see that the features would still be detectable at $\sim 3 - 5 \times 10^{-11} \text{ M}_\odot \text{ yr}^{-1}$ (green and orange lines) in all geometries considered. For the M3 stars, the lowest detectable mass accretion rate is $\sim 1 - 3 \times 10^{-11} \text{ M}_\odot \text{ yr}^{-1}$ (i.e., red and green lines).

The situation is more complicated in the real observations since chromospheric contributions could vary from object to object. However, if the accretion rates are truly low (but higher than $\sim 10^{-12} \text{ M}_\odot \text{ yr}^{-1}$), the redshifted absorption will be very evident, as seen in all cases in Figure 8. These absorption features are much broader than the typical width of the chromospheric lines (Figure 8, Table 4), and therefore accretion will still be detectable as long as the spectra are obtained at a sufficiently high resolution (we used $R=32500$, i.e., that of MIKE, in Figure 8).

The results from the two stars can also be approximately extrapolated; that is, the limit would be slightly lower than $3 \times 10^{-11} \text{ M}_\odot \text{ yr}^{-1}$ for a spectral type later than M3, and slightly higher than $5 \times 10^{-11} \text{ M}_\odot \text{ yr}^{-1}$ for a spectral type earlier than K5.

4.4. How does accretion stop?

The analysis and discussion in previous sub-sections have provided some evidence of how accretion stops. In § 4.1, we can see that essentially all low accretors are accreting in the unstable regime, but none is close to the propeller regime. Therefore, we can infer that accretion does not stop by the stellar rotation reaching the propeller regime, or at least that this process is not the main driver stopping accretion. Instead, other processes must be at play.

As discussed by Thanathibodee et al. (2020) in the study of the PDS 70 system, the formation of giant planets may, in some way, contribute to decrease accretion onto the star. However, as shown in that work, the mass accretion rates of the two planets are very small compared to that of the host star, and therefore mass accretion onto planets is unlikely to be the main source stopping accretion. Nevertheless, the formation of giant planets creates large gaps in the protoplanetary disk; this could make disk dispersal processes such as photo-evaporation become more pronounced (Alexander et al. 2014).

The fact that most of the stars in our sample are accreting at $\sim 10^{-10} \text{ M}_\odot \text{ yr}^{-1}$ even though the model can essentially detect accretion an order of magnitude lower than that suggests that we have obtained a physical lower limit to the mass accretion rate in the mass range covered by the stars in our sample. Two possibilities may be able to explain this observational result.

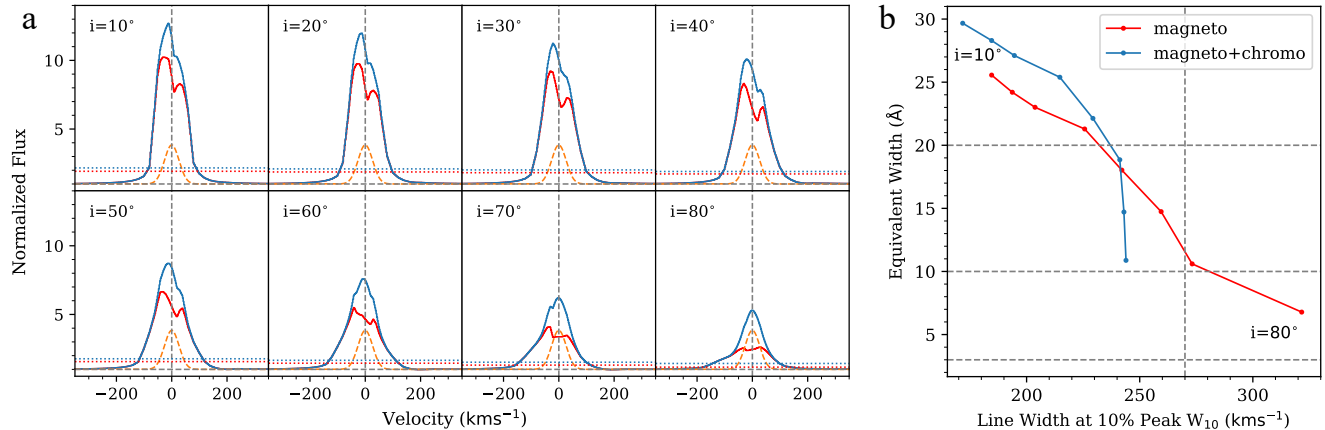


Figure 7. Changes in line strength and morphology due to inclination. We adopted the stellar parameters of the M2 star CVSO 156 with model parameters $R_i=2.6 R_*$, $W_r=0.4 R_*$, $\dot{M}=9 \times 10^{-11} M_\odot \text{ yr}^{-1}$, and $T_{\text{max}}=1.15 \times 10^4 \text{ K}$. (a) The line profiles at different inclinations from $i = 10^\circ$ to $i = 80^\circ$. The red lines are the profiles of the magnetospheric model. The orange lines are the chromospheric contribution, assumed to be constant for all inclinations. The blue lines are the sum of the two components. The dotted horizontal lines show the level at 10% of the peak flux. (b) The equivalent width and the width at the 10% flux (W_{10}) corresponding to the profiles in (a). The same color scheme is used. The points at the upper left of the plot are those with low inclinations, and the points at the lower right are at high inclinations. The horizontal lines are the accretor EW thresholds for spectral type K5, M2.5, and M5.5, and the vertical line is the W_{10} threshold of 270 km s^{-1} (White & Basri 2003).

First, it is possible that this is a selection bias, such that we only selected stars classified as accretors using the He I $\lambda 10830$ line, and that the line is not sensitive below $10^{-10} M_\odot \text{ yr}^{-1}$. Therefore, we have missed stars accreting at $\sim 10^{-11} M_\odot \text{ yr}^{-1}$. Continuous monitoring of possible accretors (c.f., Paper I) could be used to explore this possibility.

One implication of the sensitivity problem is that we cannot rule out the possibility that the inner disk could host a gas reservoir with low viscosity (Hartmann & Bae 2018). In this case, the inner disk is first separated from the outer disk due to processes that deplete the outer disk (e.g., photoevaporation). Due to low viscosity, the inner disk will drain slowly and will last long. The mass accretion rate onto the star will decrease with time, and with a sufficiently sensitive probe, accretion could be detected at the level well below $10^{-10} M_\odot \text{ yr}^{-1}$. If $\sim 10^{-10} M_\odot \text{ yr}^{-1}$ is the physical limit, the inner disk mass reservoir scenario can be reconciled with other processes removing gas from the disk, such as MHD winds launching from the inner disk (Hartmann & Bae 2018; Tabone et al. 2022a,b).

Second, it is also possible that $10^{-10} M_\odot \text{ yr}^{-1}$ is the actual limit to the rate at which a star can accrete mass from its inner disk. If the inner disk depletion timescale is short (due to, e.g., high viscosity), the mass accreted onto the star is then essentially controlled by the supply of mass from the outer disk. In this scenario, photoevaporation could play a crucial role, since photoevaporation models suggest that mass accretion onto the stars ceases in a very short time scale ($\sim 10^5 \text{ yr}$) once the mass accretion rates equal the photoevaporative mass loss rates. With the steady supply of mass from the outer disk, con-

trolled by the photoevaporative rate, our results suggest that the photoevaporative mass loss rates should not be higher than $1 \times 10^{-10} M_\odot \text{ yr}^{-1}$ for the mass range considered in this study ($0.1 - 1.2 M_\odot$) at the last stages of disk evolution.

Models of photoevaporation as well as observational constraints suggest a wide range of photoevaporative mass loss rates from $\sim 10^{-10} M_\odot \text{ yr}^{-1}$ to $10^{-8} M_\odot \text{ yr}^{-1}$, depending on which energy range dominates the disk irradiation (EUV, X-ray, or FUV; Clarke et al. 2001, Owen et al. 2011, Gorti & Hollenbach 2009). Our results agree with the low rates of mass accretion predicted by EUV-dominated photoevaporation, suggesting that it is likely the main mechanism depleting disks at their last stages of evolution. It is possible that the higher mass loss rates from other mechanism are needed at earlier stages of disk evolution, as the disk lifetime would be longer than observed if the EUV-dominated photoevaporation operates alone at all timescales (Alexander et al. 2014).

Regardless of the mechanism removing mass from the disk, it is now quite clear that mass accretion onto the star stops due to the properties of the disk as opposed to those directly related to the stars, as previously suggested in Paper I. It is possible that accretion stops because the disk simply runs out of gas, but the process of removing mass from the disk and essentially stopping accretion, remains unclear. Detailed studies of disk properties (e.g., density, mass, gap sizes, dust settling) and their related radiation fields (FUV, X-ray) are needed to pinpoint the most probable processes stopping accretion. This is a subject for a follow-up study.

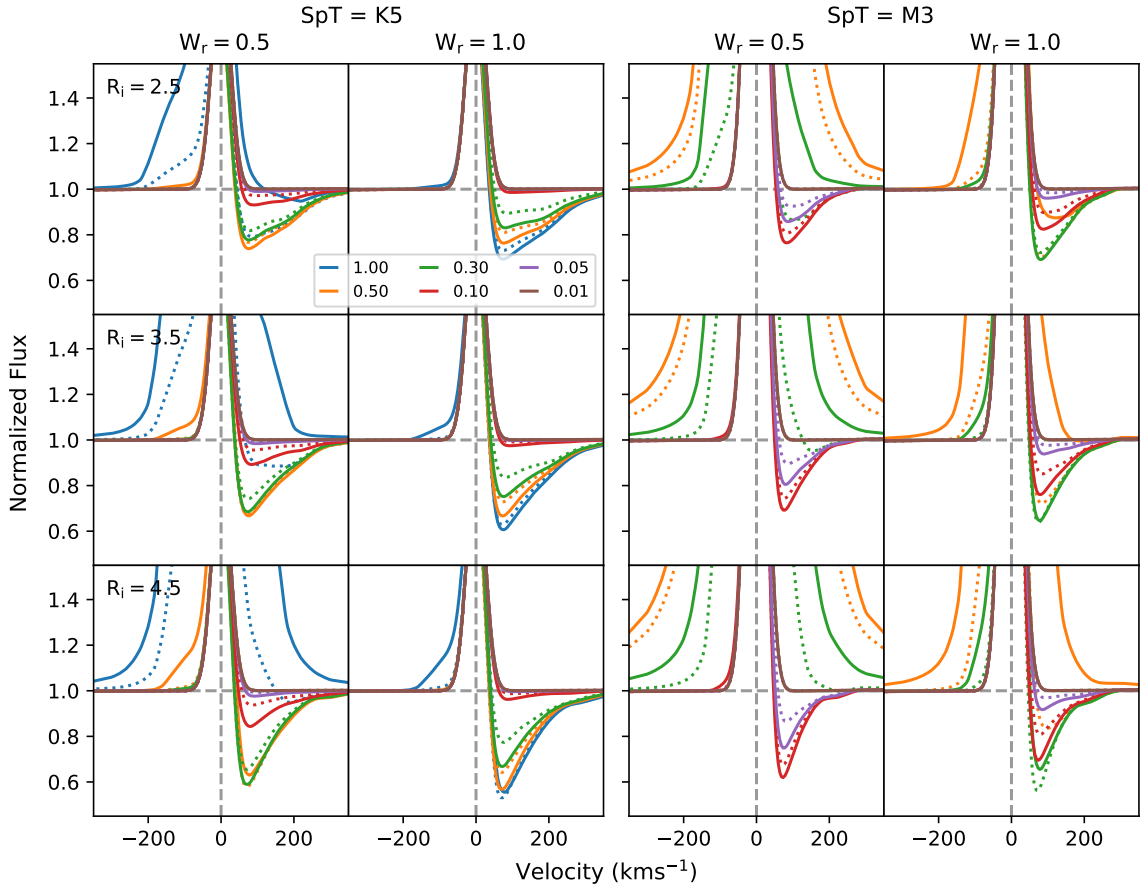


Figure 8. The variation of line profiles at the lowest limit of accretion for stars with spectral types K5 and M3. The two columns for each spectral type are for $W_r=0.5$ and $W_r=1.0$, respectively. Each row corresponds to a fixed truncation radius R_i . Different colors are for different mass accretion rates; the legend shows the mass accretion rates in units of $10^{-10} M_{\odot} \text{ yr}^{-1}$. The solid lines are the profiles calculated for $T_{\text{max}}=13,000 \text{ K}$ and the dotted lines are for $T_{\text{max}}=12,000 \text{ K}$. The black dash-dotted lines are the assumed chromospheric profiles. The range of the y-axis is fixed at low values to focus on the feature of the line near the continuum. The model at $\dot{M} = 10^{-12} M_{\odot} \text{ yr}^{-1}$, shown in brown, can barely be distinguishable from the chromosphere.

5. SUMMARY AND CONCLUSIONS

In this paper, we conducted a study of 22 accretors and two possible accretors identified as such using the profiles of He I $\lambda 10830$ line. We applied the magnetospheric accretion model (Hartmann et al. 1994; Muzerolle et al. 1998, 2001) to fit the H α lines of the stars observed with moderate resolution spectrograph and inferred the accretion properties from the best fitting models. We summarize our findings as follows:

1. Most of the H α lines have significant contributions from the narrow chromospheric emission component of the line, up to 60% in some cases and $\sim 30\%$ on average. Representing the chromospheric emission with a Gaussian, we find that 20 stars can be fitted very well with the combined magnetospheric+chromospheric model. These stars are used for further analysis.

2. A fraction of stars show low-velocity redshifted absorption on top of bright emission in the H α line profile. We speculate that the magnetospheres of these stars are similar to that of CVSO 1335 (Thanathibodee et al. 2019), where accretion occurs in a complex, multi-flows geometry.
3. We find an anticorrelation between the disk truncation radius and the mass accretion rates in the M-type stars of the sample. The power-law relation is consistent with theory and simulations within the uncertainty.
4. The disk truncation radius and the mass accretion rates are not correlated in our small sample of K-type stars. If this relationship is confirmed by larger sample size, the result may suggest departures of the magnetic field from dipolar geometry in K-type low accretors.

5. We calculated corotation radii from the projected rotational velocity of the stars and found them to be always larger than the truncation radii, which implies that the magnetic propeller is not the main agent stopping accretion. We also find that essentially all low accretors accrete in the unstable regime.
6. We compared the magnetic radius calculated from mass accretion rates and stellar parameters with the truncation radius inferred from the model and found that either the efficiency parameter ξ or the dipolar magnetic field B need to be small for the two radii to be the same. For the efficiency parameters to be comparable to other studies, the dipole magnetic field must be much weaker than the total magnetic fields, assumed to be at a few kG. This suggests that, as stars evolve, most of the magnetic fields are in higher-order configurations, but the dipole component can still truncate the disk due to the low accretion rates.
7. The inferred high inclinations of the majority of our targets suggest a possible observational bias introduced by adopting the equivalent width of $H\alpha$ as a selection criterion to identify low accretor candidates. This is because the equivalent width of the line depends strongly on the inclination for low accretors, such that it will often go below the threshold at high inclinations. Therefore, more low accretor candidates get selected at high inclinations.
8. Stars at low inclinations may also be susceptible to accretion misclassification since the chromospheric contribution to the emission is expected to be higher than in higher inclination stars. The chromospheric component may dominate subtle features (e.g., broad wings, weak absorption) of the magnetosphere.
9. Mass accretion rates of low accretors are not much lower than $1 \times 10^{-10} M_{\odot} \text{ yr}^{-1}$, regardless of the mass of the star, even though we could detect rates 5 to 10 times lower. This suggests that photoevaporative mass loss rates are of the same order, since otherwise these low accretion rates would not have been detected. This value for the photoevaporative rate is consistent with the low end of EUV-driven photoevaporation. As we ruled out the propeller as the main driver stopping accretion, the same mass accretion rates across the mass range suggest that the processes that stop mass accretion onto the star occur in the disk. It is possible that accretion stops simply because the disk runs out of gas.

We thank the anonymous referee for the helpful comments and suggestions which improve the quality of the manuscript. We thank Lee Hartmann for his useful suggestions. We are grateful to Mario Mateo for coordinating the scheduling of the MIKE observations, and to the staff at Las Campanas Observatory, in face of the partial observatory closure due to the COVID-19 pandemic. This project is supported in part by NASA grant NNX17AE57G. JH acknowledges support from program UNAM-DGAPA-PAPIIT grant IA102319.

This paper is based on data obtained from the ESO Science Archive Facility. This research made use of Astropy,¹ a community-developed core Python package for Astronomy (Astropy Collaboration et al. 2013; Price-Whelan et al. 2018).

Facilities: Magellan:Clay (MIKE), ESO:VLT (UVES, X-shooter)

Software: CarPy, Astropy (Astropy Collaboration et al. 2013; Price-Whelan et al. 2018)

REFERENCES

- Alcalá, J. M., Manara, C. F., Natta, A., et al. 2017, *A&A*, 600, A20, doi: [10.1051/0004-6361/201629929](https://doi.org/10.1051/0004-6361/201629929)
- Alencar, S. H. P., Bouvier, J., Walter, F. M., et al. 2012, *A&A*, 541, A116, doi: [10.1051/0004-6361/201118395](https://doi.org/10.1051/0004-6361/201118395)
- Alexander, R., Pascucci, I., Andrews, S., Armitage, P., & Cieza, L. 2014, in *Protostars and Planets VI*, ed. H. Beuther, R. S. Klessen, C. P. Dullemond, & T. Henning, 475, doi: [10.2458/azu_uapress.9780816531240-ch021](https://doi.org/10.2458/azu_uapress.9780816531240-ch021)
- Antoniucci, S., Nisini, B., Giannini, T., et al. 2017, *A&A*, 599, A105, doi: [10.1051/0004-6361/201629683](https://doi.org/10.1051/0004-6361/201629683)
- Astropy Collaboration, Robitaille, T. P., Tollerud, E. J., et al. 2013, *A&A*, 558, A33, doi: [10.1051/0004-6361/201322068](https://doi.org/10.1051/0004-6361/201322068)
- Batalha, C. C., Stout-Batalha, N. M., Basri, G., & Terra, M. A. O. 1996, *ApJS*, 103, 211, doi: [10.1086/192275](https://doi.org/10.1086/192275)
- Blinova, A. A., Romanova, M. M., & Lovelace, R. V. E. 2016, *MNRAS*, 459, 2354, doi: [10.1093/mnras/stw786](https://doi.org/10.1093/mnras/stw786)
- Boggs, P. T., Byrd, R. H., & Schnabel, R. B. 1987, *SIAM Journal on Scientific and Statistical Computing*, 8, 1052, doi: [10.1137/0908085](https://doi.org/10.1137/0908085)
- Chen, W., & Johns-Krull, C. M. 2013, *ApJ*, 776, 113, doi: [10.1088/0004-637X/776/2/113](https://doi.org/10.1088/0004-637X/776/2/113)

- Clarke, C. J., Gendrin, A., & Sotomayor, M. 2001, *MNRAS*, 328, 485, doi: [10.1046/j.1365-8711.2001.04891.x](https://doi.org/10.1046/j.1365-8711.2001.04891.x)
- Dahm, S. E., Slesnick, C. L., & White, R. J. 2012, *ApJ*, 745, 56, doi: [10.1088/0004-637X/745/1/56](https://doi.org/10.1088/0004-637X/745/1/56)
- Donati, J. F., Bouvier, J., Walter, F. M., et al. 2011, *MNRAS*, 412, 2454, doi: [10.1111/j.1365-2966.2010.18069.x](https://doi.org/10.1111/j.1365-2966.2010.18069.x)
- Frasca, A., Biazzo, K., Lanzafame, A. C., et al. 2015, *A&A*, 575, A4, doi: [10.1051/0004-6361/201424409](https://doi.org/10.1051/0004-6361/201424409)
- Ghosh, P., & Lamb, F. K. 1979, *ApJ*, 232, 259, doi: [10.1086/157285](https://doi.org/10.1086/157285)
- Gilmore, G., Randich, S., Worley, C. C., et al. 2022, *A&A*, 666, A120, doi: [10.1051/0004-6361/202243134](https://doi.org/10.1051/0004-6361/202243134)
- Gorti, U., & Hollenbach, D. 2009, *ApJ*, 690, 1539, doi: [10.1088/0004-637X/690/2/1539](https://doi.org/10.1088/0004-637X/690/2/1539)
- Gregory, S. G., Matt, S. P., Donati, J. F., & Jardine, M. 2008, *MNRAS*, 389, 1839, doi: [10.1111/j.1365-2966.2008.13687.x](https://doi.org/10.1111/j.1365-2966.2008.13687.x)
- Hartmann, L., & Bae, J. 2018, *MNRAS*, 474, 88, doi: [10.1093/mnras/stx2775](https://doi.org/10.1093/mnras/stx2775)
- Hartmann, L., Herczeg, G., & Calvet, N. 2016, *ARA&A*, 54, 135, doi: [10.1146/annurev-astro-081915-023347](https://doi.org/10.1146/annurev-astro-081915-023347)
- Hartmann, L., Hewett, R., & Calvet, N. 1994, *ApJ*, 426, 669, doi: [10.1086/174104](https://doi.org/10.1086/174104)
- Husser, T.-O., Wende-von Berg, S., Dreizler, S., et al. 2013, *A&A*, 553, A6, doi: [10.1051/0004-6361/201219058](https://doi.org/10.1051/0004-6361/201219058)
- Ireland, L. G., Zanni, C., Matt, S. P., & Pantolmos, G. 2021, *ApJ*, 906, 4, doi: [10.3847/1538-4357/abc828](https://doi.org/10.3847/1538-4357/abc828)
- James, D. J., Melo, C., Santos, N. C., & Bouvier, J. 2006, *A&A*, 446, 971, doi: [10.1051/0004-6361:20053900](https://doi.org/10.1051/0004-6361:20053900)
- Jönsson, H., Holtzman, J. A., Allende Prieto, C., et al. 2020, *AJ*, 160, 120, doi: [10.3847/1538-3881/aba592](https://doi.org/10.3847/1538-3881/aba592)
- Karim, M. T., Stassun, K. G., Briceño, C., et al. 2016, *AJ*, 152, 198, doi: [10.3847/0004-6256/152/6/198](https://doi.org/10.3847/0004-6256/152/6/198)
- Kelson, D. D. 2003, *PASP*, 115, 688, doi: [10.1086/375502](https://doi.org/10.1086/375502)
- Kelson, D. D., Illingworth, G. D., van Dokkum, P. G., & Franx, M. 2000, *ApJ*, 531, 159, doi: [10.1086/308445](https://doi.org/10.1086/308445)
- Kulkarni, A. K., & Romanova, M. M. 2013, *MNRAS*, 433, 3048, doi: [10.1093/mnras/stt945](https://doi.org/10.1093/mnras/stt945)
- Kurosawa, R., Romanova, M. M., & Harries, T. J. 2011, *MNRAS*, 416, 2623, doi: [10.1111/j.1365-2966.2011.19216.x](https://doi.org/10.1111/j.1365-2966.2011.19216.x)
- Lavail, A., Kochukhov, O., & Hussain, G. A. J. 2019, *A&A*, 630, A99, doi: [10.1051/0004-6361/201935695](https://doi.org/10.1051/0004-6361/201935695)
- Lavail, A., Kochukhov, O., Hussain, G. A. J., et al. 2017, *A&A*, 608, A77, doi: [10.1051/0004-6361/201731889](https://doi.org/10.1051/0004-6361/201731889)
- Lima, G. H. R. A., Alencar, S. H. P., Calvet, N., Hartmann, L., & Muzerolle, J. 2010, *A&A*, 522, A104, doi: [10.1051/0004-6361/201014490](https://doi.org/10.1051/0004-6361/201014490)
- Long, M., Romanova, M. M., & Lovelace, R. V. E. 2007, *MNRAS*, 374, 436, doi: [10.1111/j.1365-2966.2006.11192.x](https://doi.org/10.1111/j.1365-2966.2006.11192.x)
- Manara, C. F., Fedele, D., Herczeg, G. J., & Teixeira, P. S. 2016, *A&A*, 585, A136, doi: [10.1051/0004-6361/201527224](https://doi.org/10.1051/0004-6361/201527224)
- Manara, C. F., Frasca, A., Alcalá, J. M., et al. 2017a, *A&A*, 605, A86, doi: [10.1051/0004-6361/201730807](https://doi.org/10.1051/0004-6361/201730807)
- Manara, C. F., Testi, L., Rigliaco, E., et al. 2013, *A&A*, 551, A107, doi: [10.1051/0004-6361/201220921](https://doi.org/10.1051/0004-6361/201220921)
- Manara, C. F., Testi, L., Herczeg, G. J., et al. 2017b, *A&A*, 604, A127, doi: [10.1051/0004-6361/201630147](https://doi.org/10.1051/0004-6361/201630147)
- Muzerolle, J., Calvet, N., & Hartmann, L. 1998, *ApJ*, 492, 743, doi: [10.1086/305069](https://doi.org/10.1086/305069)
- . 2001, *ApJ*, 550, 944, doi: [10.1086/319779](https://doi.org/10.1086/319779)
- Owen, J. E., Ercolano, B., & Clarke, C. J. 2011, *MNRAS*, 412, 13, doi: [10.1111/j.1365-2966.2010.17818.x](https://doi.org/10.1111/j.1365-2966.2010.17818.x)
- Price-Whelan, A. M., Sipőcz, B. M., Günther, H. M., et al. 2018, *AJ*, 156, 123, doi: [10.3847/1538-3881/aabc4f](https://doi.org/10.3847/1538-3881/aabc4f)
- Romanova, M. M., Blinova, A. A., Ustyugova, G. V., Koldoba, A. V., & Lovelace, R. V. E. 2018, *NewA*, 62, 94, doi: [10.1016/j.newast.2018.01.011](https://doi.org/10.1016/j.newast.2018.01.011)
- Romanova, M. M., Kulkarni, A. K., & Lovelace, R. V. E. 2008, *ApJL*, 673, L171, doi: [10.1086/527298](https://doi.org/10.1086/527298)
- Romanova, M. M., Ustyugova, G. V., Koldoba, A. V., & Lovelace, R. V. E. 2004, *ApJ*, 610, 920, doi: [10.1086/421867](https://doi.org/10.1086/421867)
- Romanova, M. M., Ustyugova, G. V., Koldoba, A. V., Wick, J. V., & Lovelace, R. V. E. 2003, *ApJ*, 595, 1009, doi: [10.1086/377514](https://doi.org/10.1086/377514)
- Serna, J., Hernandez, J., Kounkel, M., et al. 2021, *ApJ*, 923, 177, doi: [10.3847/1538-4357/ac300a](https://doi.org/10.3847/1538-4357/ac300a)
- Tabone, B., Rosotti, G. P., Cridland, A. J., Armitage, P. J., & Lodato, G. 2022a, *MNRAS*, 512, 2290, doi: [10.1093/mnras/stab3442](https://doi.org/10.1093/mnras/stab3442)
- Tabone, B., Rosotti, G. P., Lodato, G., et al. 2022b, *MNRAS*, 512, L74, doi: [10.1093/mnrasl/slab124](https://doi.org/10.1093/mnrasl/slab124)
- Thanathibodee, T., Calvet, N., Hernández, J., Maucó, K., & Briceño, C. 2022, *AJ*, 163, 74, doi: [10.3847/1538-3881/ac3ee6](https://doi.org/10.3847/1538-3881/ac3ee6)
- Thanathibodee, T., Calvet, N., Muzerolle, J., et al. 2019, *ApJ*, 884, 86, doi: [10.3847/1538-4357/ab4127](https://doi.org/10.3847/1538-4357/ab4127)
- Thanathibodee, T., Molina, B., Calvet, N., et al. 2020, *ApJ*, 892, 81, doi: [10.3847/1538-4357/ab77c1](https://doi.org/10.3847/1538-4357/ab77c1)
- Villebrun, F., Alecian, E., Hussain, G., et al. 2019, *A&A*, 622, A72, doi: [10.1051/0004-6361/201833545](https://doi.org/10.1051/0004-6361/201833545)
- White, R. J., & Basri, G. 2003, *ApJ*, 582, 1109, doi: [10.1086/344673](https://doi.org/10.1086/344673)